

Statistics of the Planck CMB signal in direction of gamma-ray bursts from the BATSE and BeppoSAX catalogs

M. L. Khabibullina,^{1,*} O. V. Verkhodanov,^{1,**} and V. V. Sokolov^{1,***}

¹*Special Astrophysical Observatory of RAS, Nizhnij Arkhyz, 369167 Russia*

Distribution of gamma-ray bursts (GRBs) from catalogs of the BATSE and BeppoSAX space observatories relative to the cosmic microwave background (CMB) data by Planck space mission is studied. Three methods were applied for data analysis: 1) a histogram of CMB signal values in GRB directions, 2) mosaic correlation maps calculated for GRB locations and CMB distribution, 3) calculation of an average response in the area of “an average population GRB” on the CMB map. A correlation between GRB locations and CMB fluctuations was detected which can be interpreted as systematic effects in the process of observations. Besides, in averaged areas of CMB maps, a difference between distributions of average fluctuations for short and long GRBs was detected, which can be caused by different natures of these events.

1. INTRIDUCTION

The quality of sky surveys carried out in the recent decade in different wavelength ranges permits us studying the matter distribution in the observable part of the Universe on basis of many observational effects. Beside the direct measurement of parameters of galaxy distribution and reconstruction of the large-scale structure, as was done in the SDSS survey [1], there are many effects enabling the restoration of matter distribution. Among them there are effects of the secondary CMB anisotropy: the integrated Sachs–Wolfe effect [2] caused by alteration of frequency of CMB photons in variable gravitational potential of forming galaxy clusters and prevailing on the scales $>10^\circ$, the Zeldovich–Syunaev effect [3] on the scales

* Electronic address: rita@sao.ru

** Electronic address: vo@sao.ru

*** Electronic address: sokolov@sao.ru

$<10'$ arising in interactions between hot electrons in galaxy clusters with CMB photons (the inverse Compton effect), effects of scattering in the reionization epoch, and simply the obstructive factors in the form of microwave emission of radio sources and galaxy clusters. Gamma-ray bursts are also an independent sign of the Large Scale Structure (LSS) allowing us tracing the matter distribution at cosmologic distances.

On the other hand, the observable uniform distribution of gamma-ray bursts on the projection celestial sphere, as well as the distribution of the main bulk of radio sources (excepting the faintest ones related to the nearest galaxies) demonstrates the cosmological principle requiring the Universe to be uniform and isotropic irrespective of an observer's location [4]. Observations show that the size of the largest structures is of order of 400 Mpc [5]. On lower scales, especially at low redshifts ($z < 0.1$), the matter is distributed anisotropically and inhomogeneously. However, the search for such structures continues at $z < 1$ also (e.g., see [6, 7]). Note that integral and statistical characteristics of CMB distribution determined from correlation maps with SDSS galaxy locations show the presence of the distinguished scales of 2–3 degrees within the redshift range $z = 0.8 - 2$, which corresponds to the linear scale 60 Mpc and can be interpreted as the maximum size of a heterogeneity cell [8–12]. This agrees with the model of activity of radio sources in the range $z \sim 1 - 2$ [13, 14], where variations of gravitational potential in forming clusters are expected. In this respect the comparative distribution of CMB maps extrema and GRBs on the celestial sphere is interesting as a new indicator of LSS signature on CMB maps at different redshifts. The uniform observable distribution of GRBs also enables the testing of the cosmological principle. Besides, it is assumed that they can be used as standard candles for estimation of distance to objects under consideration [15, 16]. The available rather large catalogs – BeppoSAX¹ (Satellite per Astronomia X, “Beppo” in honor of Guiseppe Occhialini) [17] and BATSE² (Burst and Transient Source Experiment) [18] comprising such objects allow us studying the spatial distribution of these objects.

In recent years, many authors investigated the gamma-ray distribution by many methods [19–25]. Paper [23] can be marked out among them. Its authors studied GRBs of short ($t < 2$ sec), medium ($(2 < t < 10$ sec) and long ($t > 10$ sec) duration from the BATSE catalog by different methods (by means of Voronoi tessellations, minimum spanning tree,

¹ <http://www.asdc.asi.it/bepposax/>

² <http://www.batse.msfc.nasa.gov/batse/>

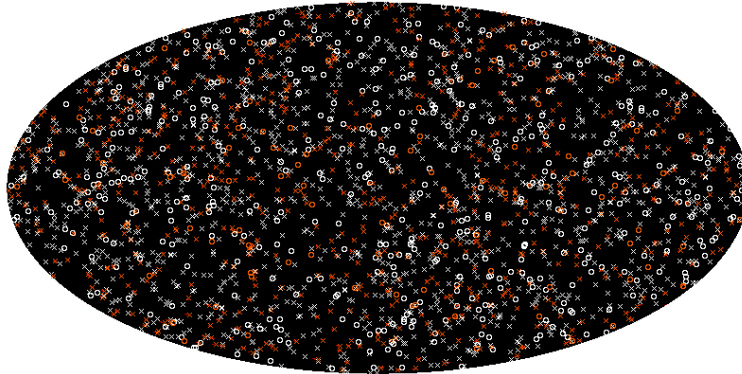


Figure 1. Distribution of gamma-ray bursts over the celestial sphere. BeppoSAX data are shown by black, those of BATSE – by white. Short bursts are denoted by circles, long bursts – by crosses.

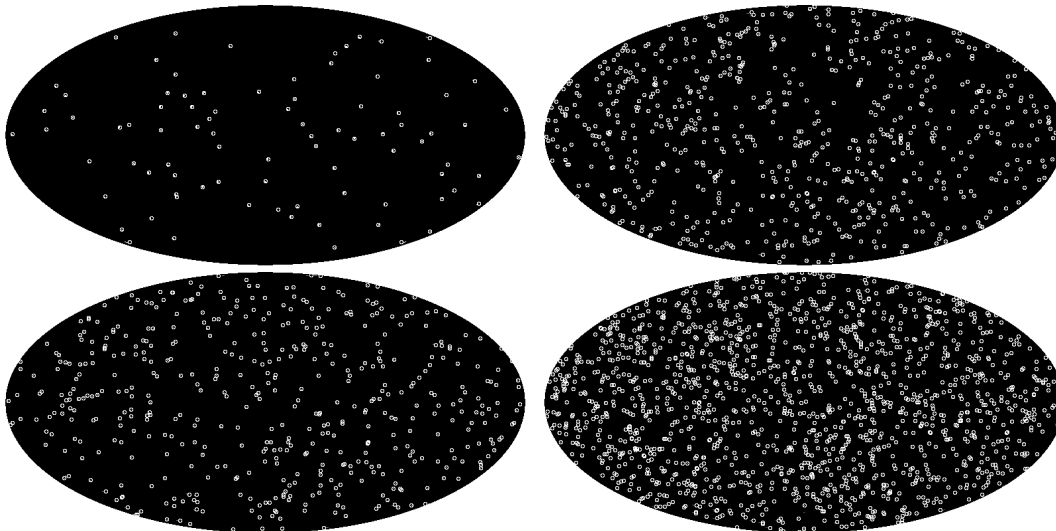


Figure 2. Distribution of GRB catalog subsamples over the celestial sphere. The top left image shows the Beppo SAX data, $t < 2$ sec. The top right image shows the BeppoSAX data, $t > 2$ sec.

The bottom left image presents the BATSE data, $t < 2$ sec. The bottom right image is for the

BATSE data, $t > 2$ sec.

(multifractal spectrum). For the first two groups, they discovered deviations from homogeneity as compared with model data. On this basis, they discuss the satisfiability of the cosmological principle. In paper [25] the locations of supernovae bursts with $z < 1.4$, as well as gamma-ray bursts, were used as probing objects. For supernovae data, a deviation from uniform distribution on the diagram “CMB temperature in a source direction – z ” was discovered in contrast to the similar diagram for gamma-ray bursts. The authors explain this difference by contribution of the integral Sachs-Wolfe effect.

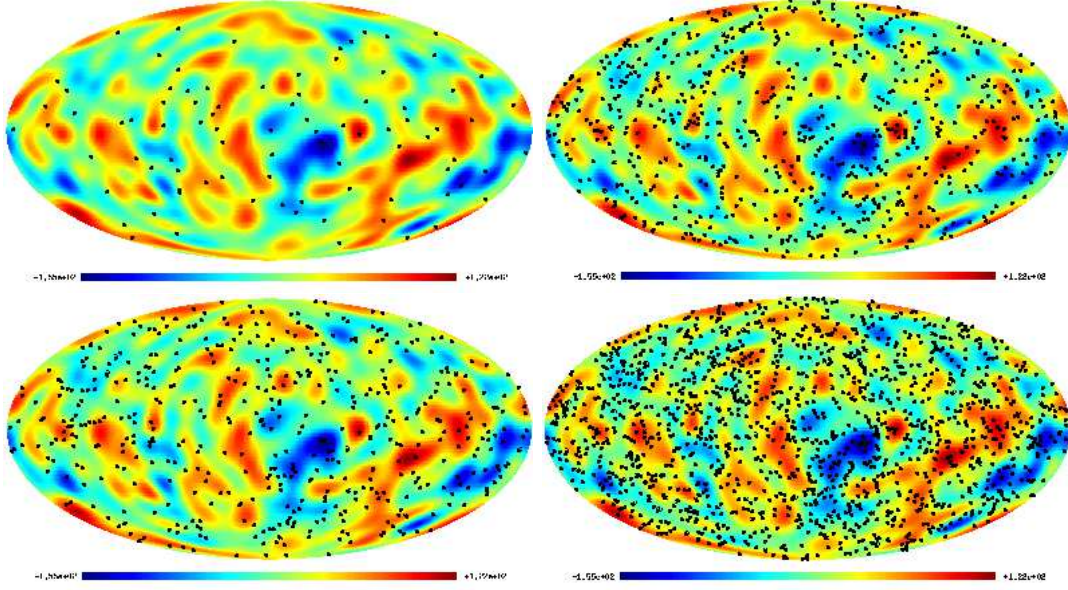


Figure 3. Location of GRBs from different samples on CMB maps with resolution $\ell_{\max} = 20$. The top left image presents the BeppoSAX data, $t < 2$ sec. The top right image shows the BeppoSAX data, $t > 2$ sec. The bottom left image presents the BATSE data, $t < 2$ sec. The bottom right image shows the BATSE data, $t > 2$ sec.

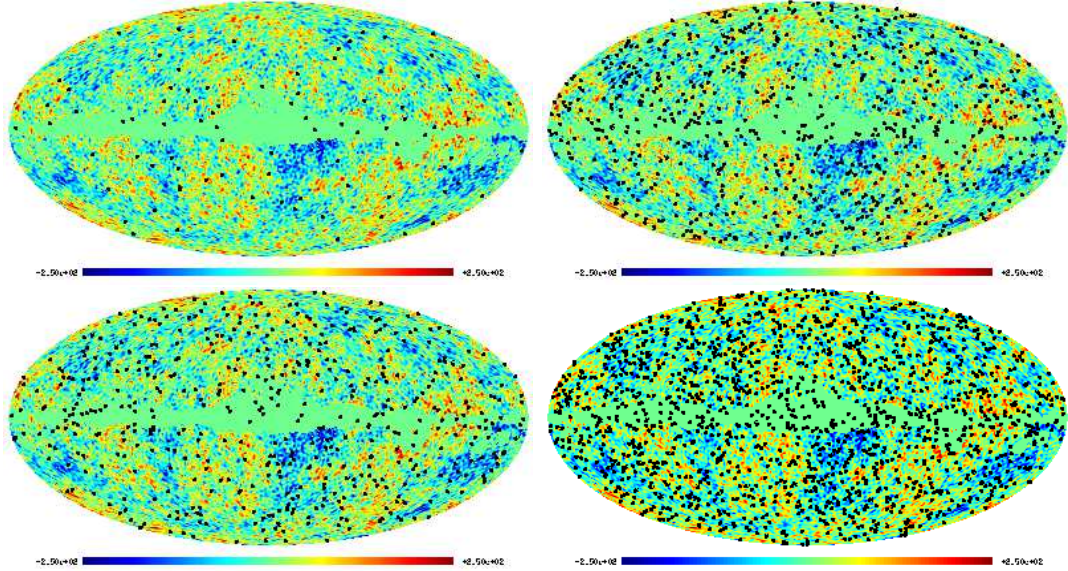


Figure 4. Location of gamma-ray bursts from different subsamples on CMB maps with the resolution $\ell_{\max} = 150$. The CMB map is masked. The top left image shows the BeppoSAX data, $t < 2$ sec. The top right image presents the BeppoSAX data, $t > 2$ sec. The bottom left image – the BATSE data, $t < 2$ sec. The bottom right image – the BATSE data, $t > 2$ sec.

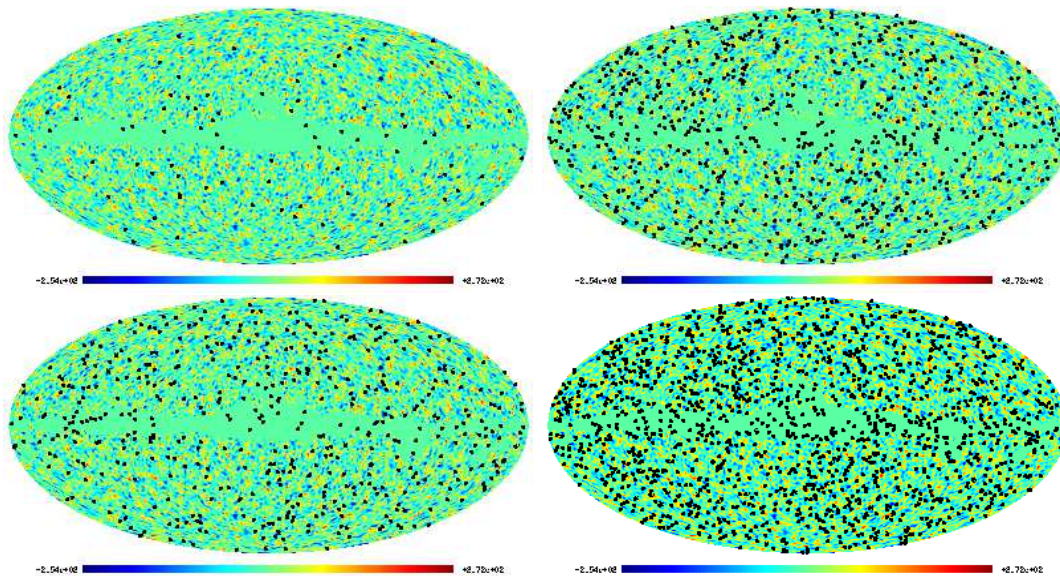


Figure 5. Location of GRBs from different subsamples on CMB maps in the multipole range $20 < \ell \leq 150$. The CMB map is masked. The top left image shows the BeppoSAX data, $t < 2$ sec. The top right image presents the BeppoSAX data, $t > 2$ sec. The bottom left image – the BATSE data, $t < 2$ sec. The bottom right image – the BATSE data, $t > 2$ sec.

In our previous paper [24], we studied statistical correlation properties of sky distribution of GRBs relative to CMB by the mosaic correlation mapping method [26, 27]. The study involved WMAP³ (Wilkinson Microwave Anisotropy Probe) data [28], data by the Italian–Dutch satellite BeppoSAX (the energy range 0.1–200 keV, 781 sources) and results of the BATSE experiment (20 keV – 2 MeV, 2037 sources). Each catalog was divided into two subsamples containing short (of duration $t < 2$ sec) and long ($t > 2$ sec) events. Figure 1 shows location of all gamma-ray bursts of the BeppoSAX and BATSE catalogs. Figure 2 presents locations of short and long GRBs from the BeppoSAX and BATSE catalogs.

If we assume that GRBs are related to massive spiral (for long GRBs) or elliptic (for short bursts) galaxies, and, respectively, their location is related to the large-scale structure, then one can study statistics of CMB inhomogeneities arising due to effects of the secondary anisotropy. Thus, the GRB locations can be related to distribution of CMB fluctuations (e.g., revealing themselves by deviations from statistical anisotropy) in projection to the sphere of regions where GRBs were registered. Since in most cases the main problem when

³ <http://lambda.gsfc.nasa.gov>

studying GRBs is the large size of error boxes in determination of source coordinates (of order of $1^\circ \times 1^\circ$), we worked with maps smoothed to 1° . Our previous work with the WMAP data resulted in discovery of a correlation between CMB peaks and GRB locations, which, in particular, can be caused by systematic effects. The detected correlation of GRB locations and CMB distribution is sensitive to the equatorial coordinate system and can be caused, for example, by the fact that the microwave radiation of the Earth gets to far side lobes of the antenna beam.

This paper continues our previous one [24], in which the data from the WMAP archives [28] were used. In this work, we applied and developed our approach for data of the Planck space mission Planck⁴ [29], specifically, for the SMICA map [30].

Below we apply several statistical approaches to study distribution of gamma-ray bursts over the sphere. Section 2 deals with CMB signal statistics in the region of GRBs. In Section 3, we investigate mosaic correlations of CMB maps (Planck SMICA) and GRB locations. Further (Section 4) we use the averaging procedure (stacking) of CMB map fields in direction of a gamma-ray burst to estimate an average “population” microwave signal. The obtained results are discussed in Conclusion.

2. STATISTICS OF CMB SIGNAL IN REGION OF GAMMA-RAY BURSTS

The SMICA map [30] of the Planck experiment CMB was restored from multifrequency observations obtained with the High Frequency Instrument (HFI) in bands at 100, 143, 217, 353, 545, 857 GHz and with the Low Frequency Instrument (LFI) in bands at 30, 44, 70 GHz. Resolution of the CMB map was $\sim 5'$. In spite of the fact that the Planck mission is secondary with respect to another NASA space mission — WMAP (Wilkinson Microwave Anisotropy Probe), its observational characteristics are better. Among them one can mark out a higher resolution (by 3 times), which gave an opportunity to measure the angular power spectrum to higher harmonics (i.e. to higher values of ℓ), a higher sensitivity (by 10 times) and 9 frequency bands improving the procedure of separation of background components. These Planck parameters allowed us obtaining new, practically independent (of WMAP) observational data. In this paper we used the SMICA map smoothed to $\ell_{\max} = 150$, and in

⁴ http://www.sciops.esa.int/wikiSI/planckpla/index.php?title=Main_Page&instance=Planck_Public_PLA

a number of cases we applied the mask Mask-RulerMinimal_2048_R1 [29].

To analyze the statistics of pixel values we used the ‘mapcut’ procedure of the GLESP package⁵ [31]. Calculations were made for the maps smoothed to the resolution 260′ ($\ell_{\max} = 20$), 35′ ($\ell_{\max} = 150$), 20′ ($\ell_{\max} = 300$) и 10′ ($\ell_{\max} = 600$). Figures 3 and 4 show the locations of GRBs from subsamples of BeppoSAX and BATSE catalogs on CMB maps with the resolution 260′ ($\ell_{\max} = 20$) and 35′ ($\ell_{\max} = 150$). The map resolution was selected in accordance with the expected scale of the Sachs–Wolfe effect manifestations and possible appearance of some features on the SMICA map. By way of example, Figure 5 shows GRB locations on the CMB map within the multipole range $20 < \ell \leq 150$.

To search for potential correlations we counted how many GRBs get to CMB pixels with negative values of signal fluctuations, which can be due to above effects on CMB maps with different resolutions. Table 1 gives the statistics of CMB pixel values in GRB locations for subsamples of BATSE and BeppoSAX catalogs for short and long events. It contains the following parameters: the total number of sources in subsamples, the amount of sources which get to CMB pixels with a negative value of fluctuations and also the expected number of pixels with a negative value of CMB amplitude by model data of 200 realizations of a Gaussian random CMB signal in the Λ CDM cosmological model and the 1σ -dispersion of these values. Data were obtained both with consideration for the Planck data and without it.

Figures 6, 7, 8, 9 present diagrams of distribution of CMB fluctuation values for four subsamples of GRBs and CMB maps with different resolutions. The dashed lines show the expected 1σ -dispersion of CMB values in the Λ CDM cosmological model. In our previous work [24] we discovered a deviation from what was expected with the Gaussian random CMB signal in distribution of fluctuation values with the resolution $\ell_{\max} = 150$ in regions of short BATSE GRBs. In the Planck data the deviations are also observed for short GRBs (see two upper diagrams in Fig. 7). Besides, there are small deviations from the models for long BATSE GRBs and short BeppoSAX GRBs at $\ell_{\max} = 20$ (the second and thirds pairs of diagrams in Fig. 6), short BeppoSAX GRBs at $\ell_{\max} = 150$ (the third diagram in Fig. 7), long BATSE GRBs at $\ell_{\max} = 300$ (the right upper diagram in Fig. 8), and long BeppoSAX GRBs at $\ell_{\max} = 600$ (the right bottom diagram in Fig. 9). To analyze the sphere distribution of

⁵ <http://www.glesp.nbi.dk>

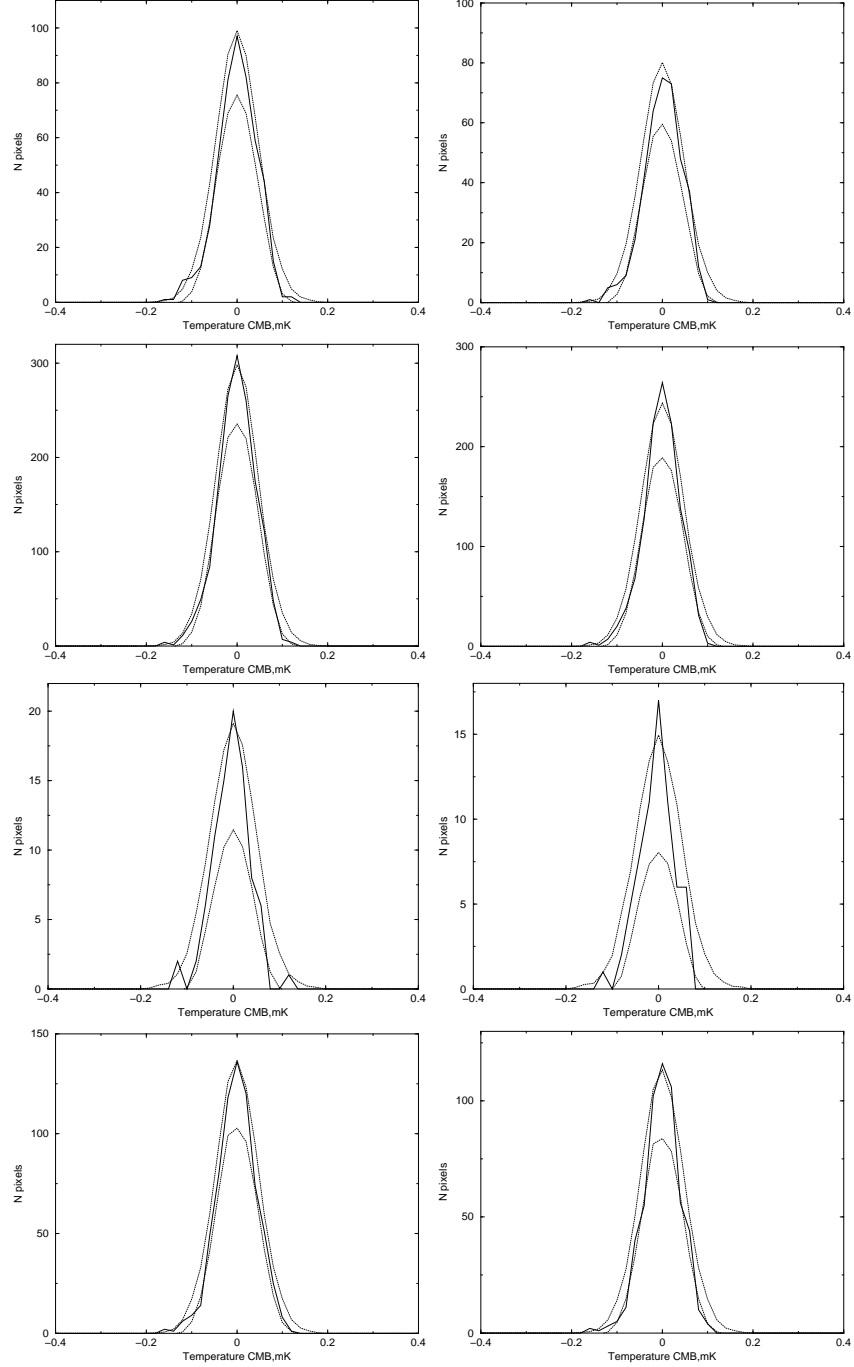


Figure 6. Distribution of CMB fluctuations values in SMICA map pixels corresponding to GRB locations with the map resolution $\ell_{\max} = 20$ for different GRB subsamples. The results without account for a mask in the SMICA map are given on the left; those with the mask are on the right. The upper pair of diagrams shows the distribution of short ($t < 2$ sec) BATSE GRBs. The second pair presents the distribution of long ($t > 2$ sec) BATSE GRBs. The third pair gives the distribution of signals for short BeppoSAX GRBs. The lowest pair — those for long BeppoSAX GRBs. The dashed lines show the 1σ -dispersion of CMB values in the Λ CDM cosmological model.

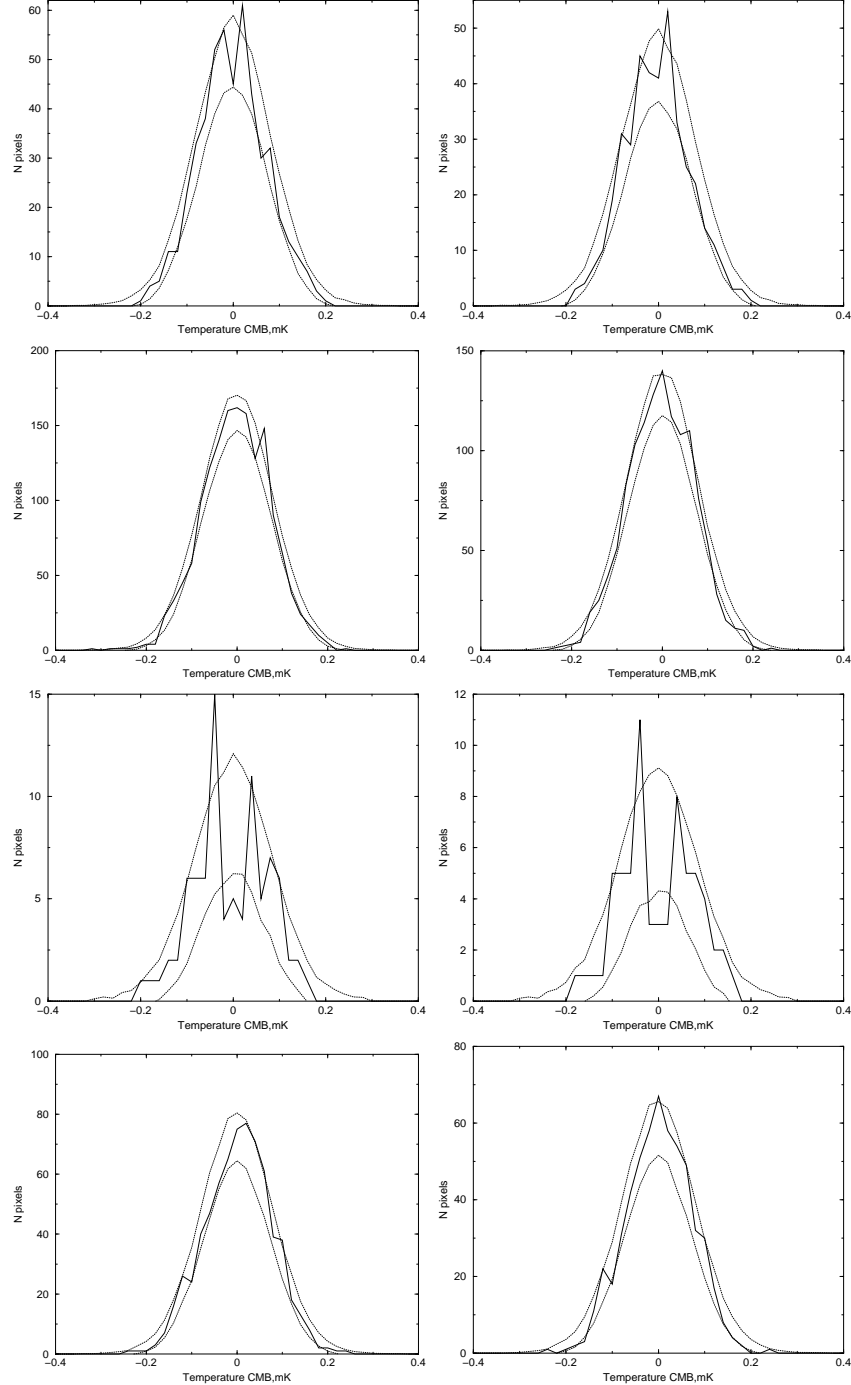


Figure 7. Distribution of CMB fluctuations in SMICA map pixels corresponding to GRB locations with the map resolution $\ell_{\max} = 150$ for different GRB subsamples. The results without account for a mask in the SMICA map are given on the left; those with the mask are on the right. The upper pair of diagrams shows the distribution of short ($t < 2$ sec) BATSE GRBs. The second pair presents the distribution of long ($t > 2$ sec) BATSE GRBs. The third pair gives the distribution of signals for short BeppoSAX GRBs. The lowest pair shows those for long BeppoSAX GRBs. The dashed lines demonstrate the 1σ -dispersion of CMB values in the Λ CDM cosmological model.

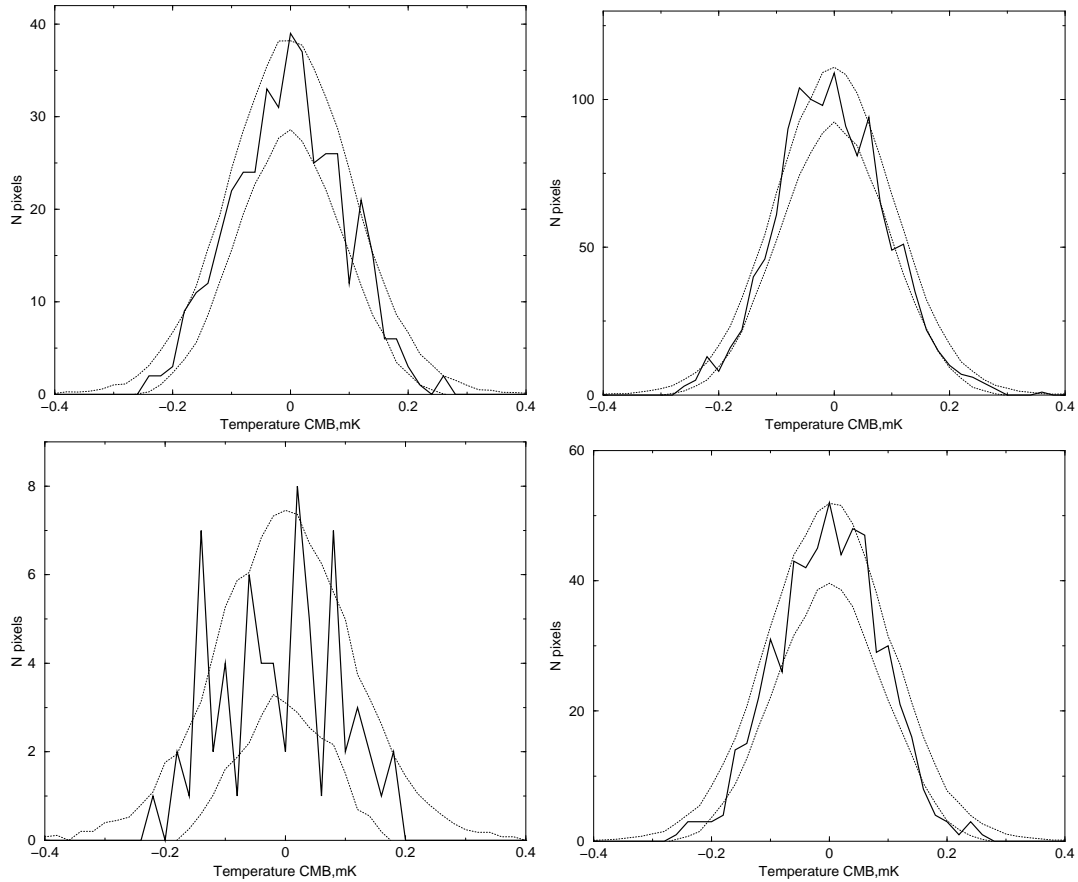


Figure 8. Distribution of CMB fluctuation values in the SMICA map pixels corresponding to GRB locations with the map resolution $\ell_{\max} = 300$ for different GRB subsamples. The results are given with the account for the mask in the SMICA map. The left upper diagrams show the statistics for short ($t < 2$ sec) BATSE GRBs. The right upper diagram presents those for long ($t > 2$ sec) BATSE GRBs. The left bottom diagram presents results for short BeppoSAX GRBs. The right bottom diagram is for long BeppoSAX events. The dashed lines show the 1σ -dispersion of CMB values in the Λ CDM cosmological model.

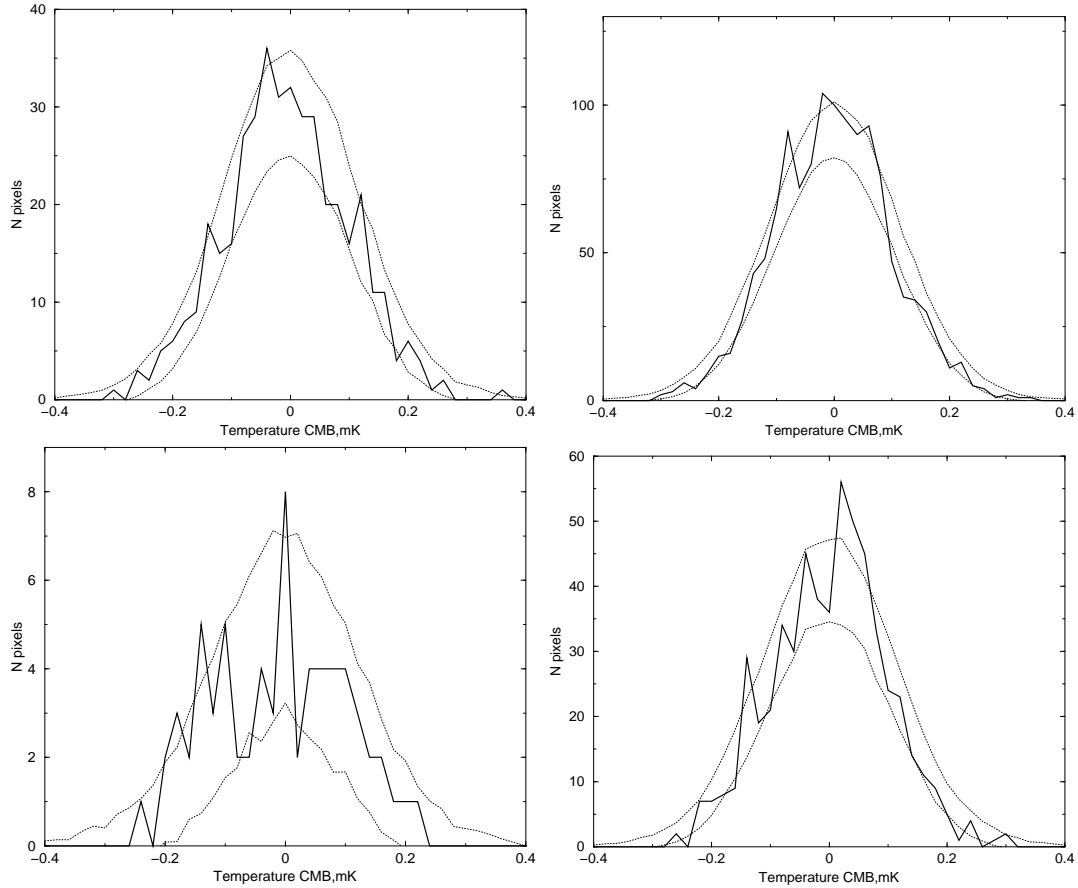


Figure 9. Distribution of CMB fluctuation values in the SMICA map pixels corresponding to GRB locations with the map resolution $\ell_{\max} = 600$ for different GRB subsamples. The results are given with the account for the mask in the SMICA map. The left upper diagram shows the statistics for short ($t < 2$ sec) BATSE GRBs. The right upper diagram presents those for long ($t > 2$ sec) BATSE rGRBs. The left bottom diagram presents results for short BeppoSAX GRBs. The right bottom diagram is for long BeppoSAX events. The dashed lines show the 1σ -dispersion of CMB values in the Λ CDM cosmological model.

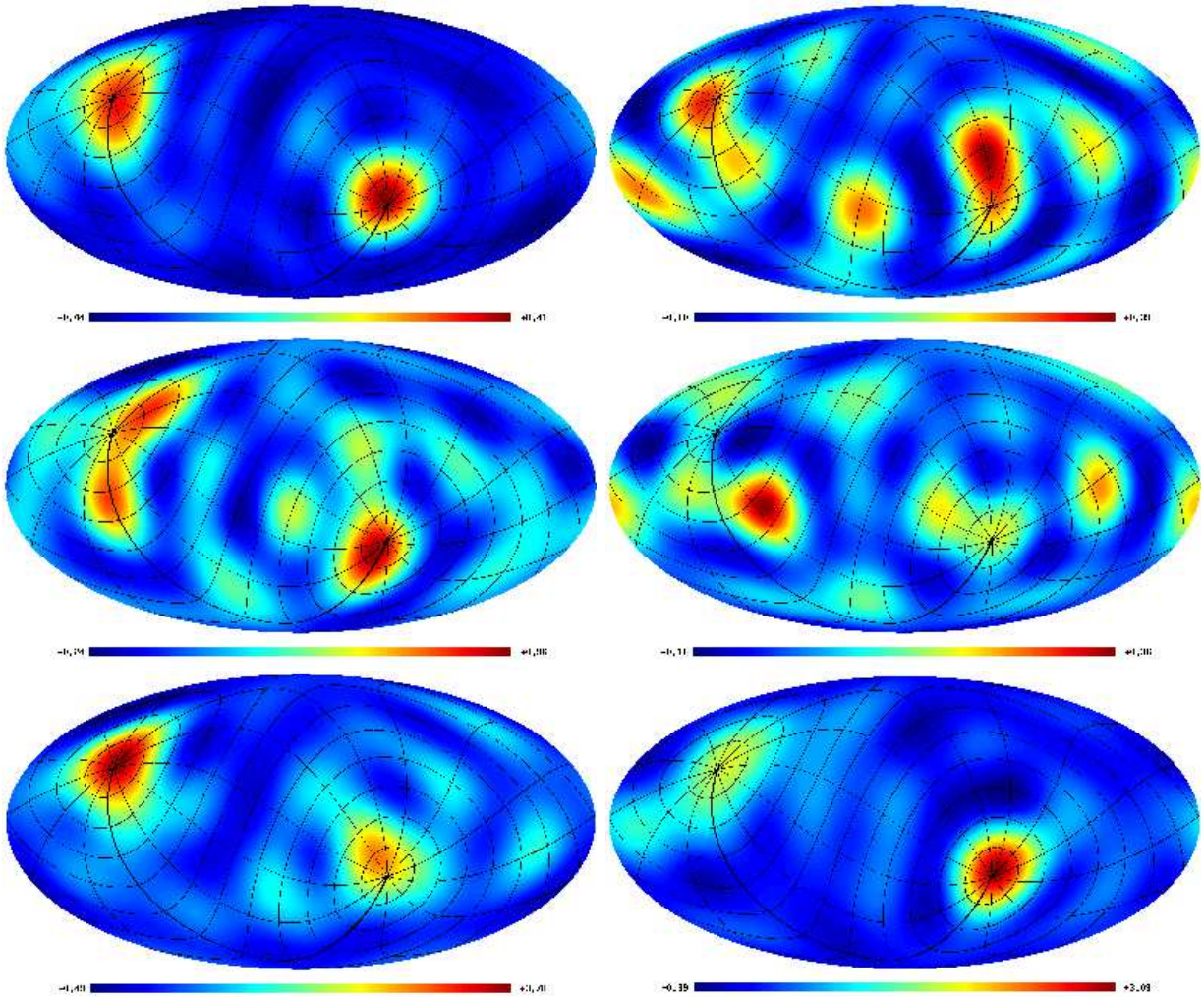


Figure 10. The smoothed maps of the sky up to $\ell_{\max} = 7$ for different GRB subsamples. The maps were built from CMB pixels corresponding to direction to those GRBs which deflect the histograms from the expected ones (see Figs. 6, 7,8,9). All maps were superimposed with the equatorial coordinate system. The upper images present data for GRBs compared with CMB in the maps with resolution $\ell_{\max} = 20$ (Fig. 6); the left one is for long BATSE GRBs, the right one is for short BeppoSAX GRBs. In the center image ($\ell_{\max} = 150$): the left one is for data of short BATSE GRBs, the right one is for short BeppoSAX GRBs. In the bottom pair of images the left one is for long BATSE GRBs ($\ell_{\max} = 300$), the right one is for long BeppoSAX GRBs ($\ell_{\max} = 600$).

Table 1. The statistics of CMB pixel values in GRB locations for BATSE and BeppoSAX subsamples. The columns are: the duration t (sec); consideration of mask in the Planck data; the mission; CMB map resolution (the multipole number); the total amount of GRB sources in a subsample (N_t), the number of sources (N_e), which are in the CMB pixels with a negative value of fluctuation; difference ΔN between N_e and expected average in random realizations; the expected amount of pixels with a negative amplitude of CMB values from data of 200 realizations of a random Gaussian signal in the Λ CDM cosmology and the 1σ dispersion of these values.

t	Mask	Mission	ℓ_{\max}	N_t	N_e	ΔN	Simulation
>2	n	BATSE	20	1540	781	12	769±32
>2	y	BATSE	20	1243	632	8	624±33
<2	n	BATSE	20	497	247	-1	248±13
<2	y	BATSE	20	394	184	-16	200±13
>2	n	BATSE	150	1540	772	4	768±19
>2	y	BATSE	150	1242	638	16	622±21
<2	n	BATSE	150	497	248	-1	249±11
<2	y	BATSE	150	403	200	-8	208±11
>2	y	BATSE	300	1248	655	33	622±21
<2	y	BATSE	300	409	207	2	205±10
>2	y	BATSE	600	1244	625	4	621±20
<2	y	BATSE	600	413	220	12	208±10
>2	n	Bepposax	20	694	343	-5	348±17
>2	y	Bepposax	20	555	272	-15	287±19
<2	n	Bepposax	20	87	44	0	44 ±5
<2	y	Bepposax	20	67	34	1	33 ±4
>2	n	Bepposax	150	694	327	-30	347±15
>2	y	Bepposax	150	562	271	-9	280±15
<2	n	Bepposax	150	87	45	1	44 ±5
<2	y	Bepposax	150	66	34	1	33 ±4
>2	y	Bepposax	300	559	279	-3	282±13
<2	y	Bepposax	300	65	32	-1	33 ±4
>2	y	Bepposax	600	563	266	-15	281±13
<2	y	Bepposax	600	68	34	0	34 ±4

those GRBs which are in directions where the detected signal deviates from the expected one, we made pixelization with the ‘mappat’ procedure from the software package GLESP [31]. The pixel size $700' \times 700'$ was chosen in such a way that the maximum pixel value (the number of events in a corresponding area) would be not less than 3 and the significant dynamic range for harmonic analysis would be provided. Fig. 10 shows so pixelized and smoothed maps of GRBs whose contribution into histogram exceeds the expected 1σ -dispersion. The equatorial coordinate system is plotted on all maps. All images demonstrate a non-uniform sphere distribution of events concentrated near the equatorial poles. In many cases, the hot spots are located directly in the equatorial poles. In maps of $\ell_{\max} = 20$ and $\ell_{\max} = 150$ with short BeppoSAX GRBs we observe clusterization of hot spots in the Galaxy plane, which is more noticeable on octupoles of these maps (Fig. 11). In some cases, the presence or absence of events in the pole regions practically repeat the pole regions of the equatorial coordinate system.

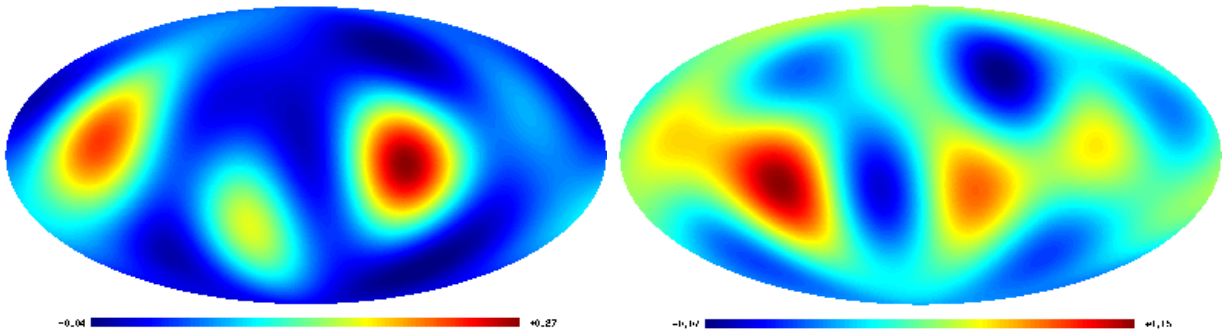


Figure 11. The octupole of the smoothed maps of the sky (Fig. 10) of short BeppoSAX GRBs locations for $\ell_{\max}=20$ and $\ell_{\max}=150$.

Note that the peculiarities of CMB data of the Planck mission are identical to those of WMAP data as compared with GRB locations. Namely, the deviations in the pixel statistics are related with signal in a GRB direction oriented in the equatorial coordinate system. In paper [24], we estimated probability of the getting of quadrupole minimums in regions of the 5° radius around the equatorial poles. To do that, we generated 10000 random realizations of the Gaussian signal to pixelize GLESP with 102 pixels in the equator. Probability of the random getting to the pole zone is 0.0035.

For a more detailed study of correlation effects, the mosaic correlation method presented in paper [26] was applied.

3. CORRELATION MAPS OF DISTRIBUTION OF GAMMA-RAY BURSTS AND PLANCK SMICA DATA

To study properties of maps of GRB locations and CMB fluctuations we fulfilled the mosaic correlation of “BATSE – CMB” maps with pixels of different sizes $500' \times 500'$, $600' \times 600'$ and $900' \times 900'$ covering areas within which the correlation factor was calculated. To do that, first we pixelized the maps of GRB locations in all four subsamples (Fig.12). As in the previous stage, the pixel size of $200' \times 200'$ was chosen in such a way that the maximum values (the number of events in a corresponding area) would be not less than 3. The correlation results are shown in Fig. 13.

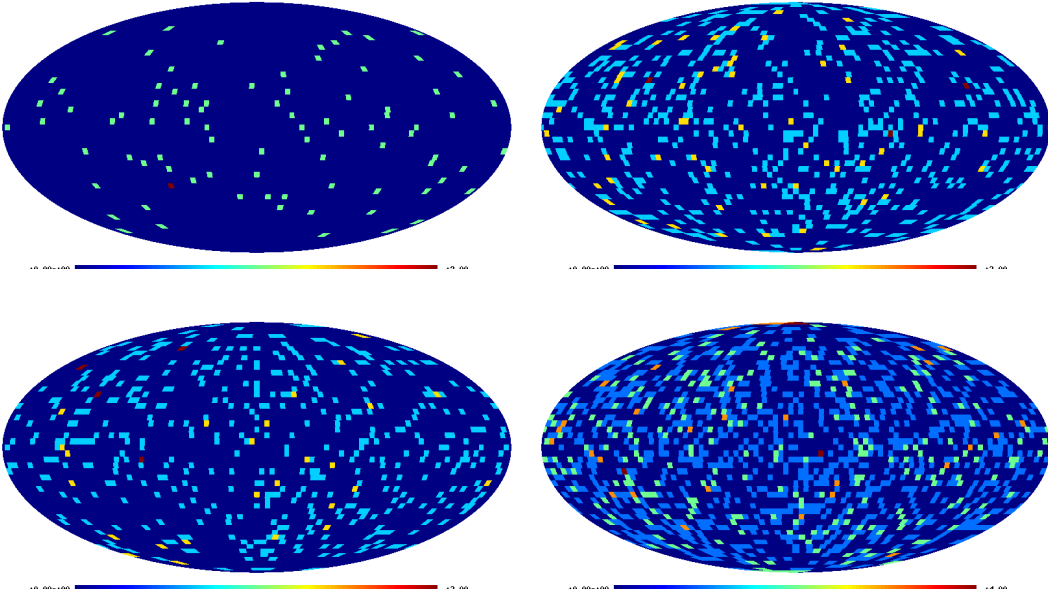


Figure 12. Pixelized maps of subsample GRB locations. The pixel size is $200' \times 200'$. The top left image shows the BeppoSAX data, $t < 2$ sec. The top right image presents the BeppoSAX data, $t > 2$ sec. The bottom left image shows the BATSE data, $t < 2$ sec. The bottom right image is for the BATSE data, $t > 2$ sec.

To analyze the obtained result we calculated the angular power spectrum of map (2) using the spherical harmonics (multipoles) expansion of signal distributed on a sphere (1):

$$\Delta S(\theta, \phi) = \sum_{\ell=1}^{\infty} \sum_{m=-\ell}^{m=\ell} a_{\ell m} Y_{\ell m}(\theta, \phi), \quad (1)$$

$$C(\ell) = \frac{1}{2\ell + 1} \left[|a_{\ell 0}|^2 + 2 \sum_{m=1}^{\ell} |a_{\ell, m}|^2 \right]. \quad (2)$$

The angular power spectrum permits us selecting harmonics contributing to the correlation map. Figs. 14,15,16 show power spectra of maps of correlation factors calculated by the mosaic correlation method for the BATSE and CMB data.

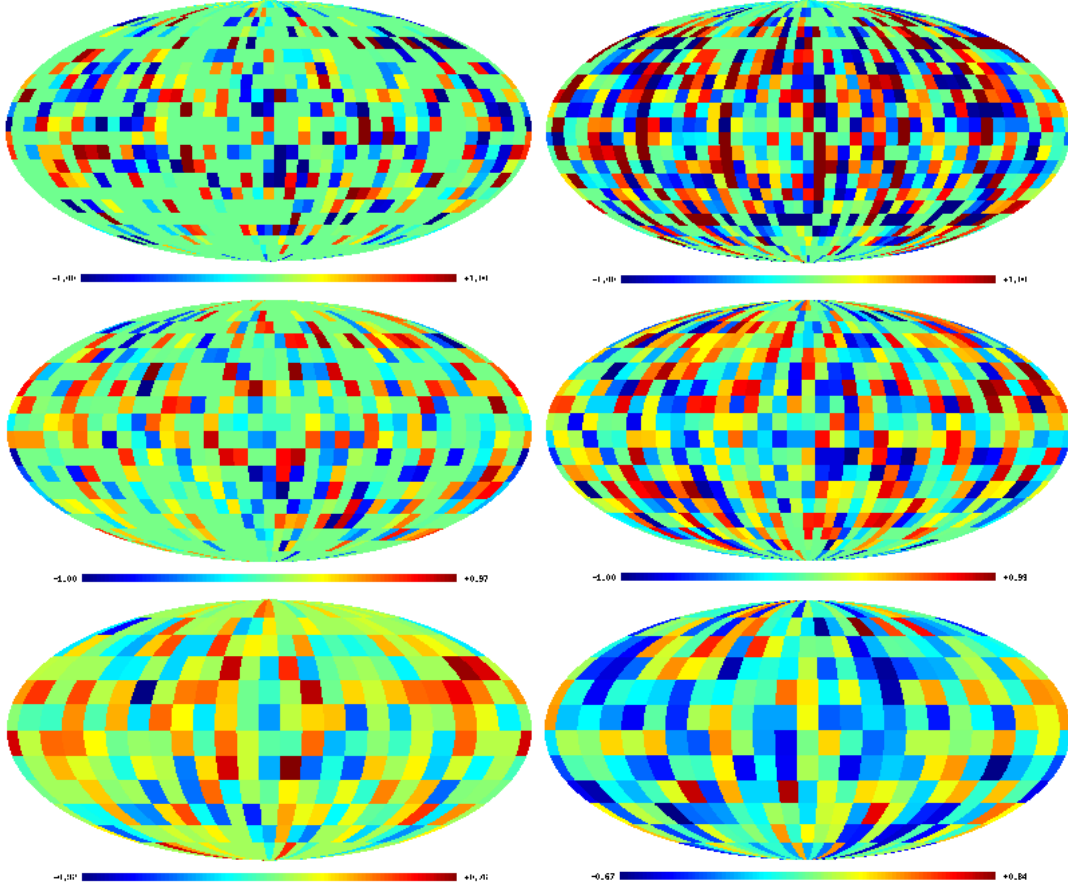


Figure 13. Correlation maps of CMB and BATSE GRB locations in the galactic coordinate system. The left column presents results of the CMB and BATSE ($t < 2$ sec) data correlations, and the right one is for CMB and BATSE ($t > 2$ sec). The upper pair of images demonstrates maps of $\ell_{\max} = 26$ and the mosaic correlation pixel size of $500' \times 500'$. The central pair of images shows the maps of $\ell_{\max} = 8$ and the mosaic correlation pixel size of $600' \times 600'$. The lower pair of images is for $\ell_{\max} = 5$ and the mosaic correlation pixel size of $900' \times 900'$.

As is shown in Figs.14, 15 and 16, application of the mask retains location of local maximums in the power spectra of mosaic maps. In a number of cases, the application of the mask even amplifies the amplitude of a distinguished harmonic. Fig.17 demonstrates

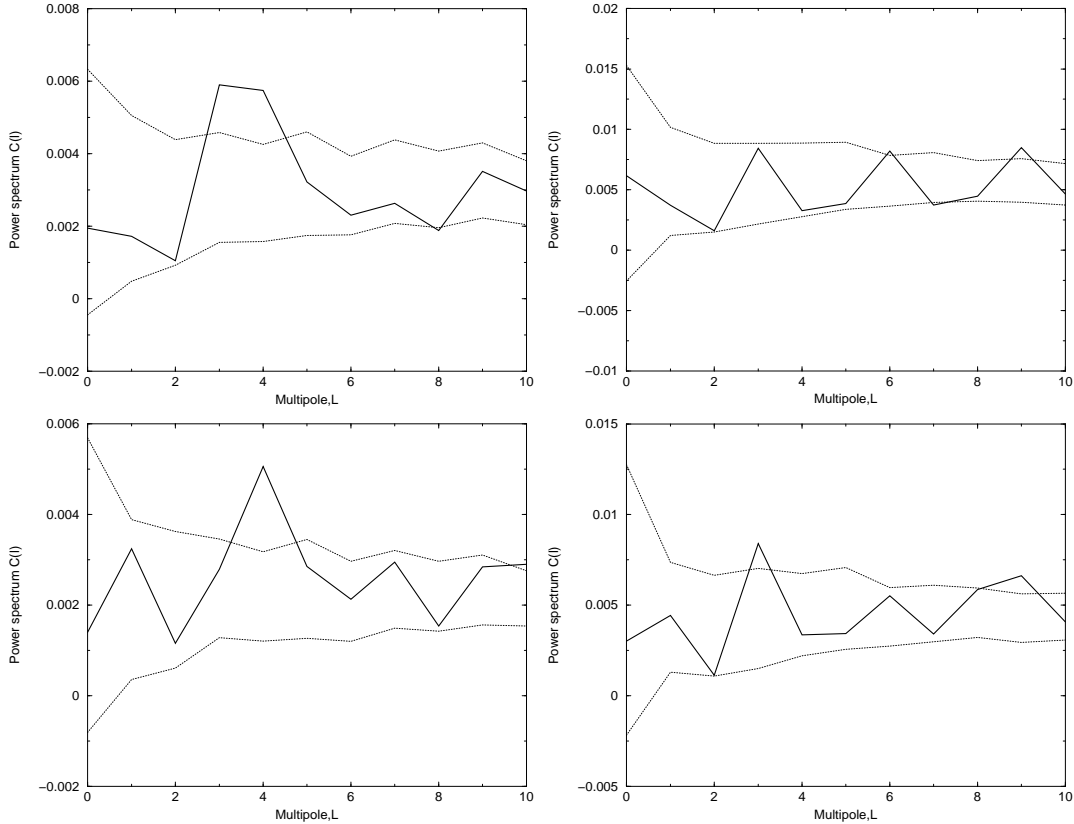


Figure 14. Power spectra of correlation factor maps (with the resolution of $\ell_{\max} = 26$) calculated for the maps of BATSE GRBs locations and CMB distribution (the solid line). The correlation pixel size is $500' \times 500'$. The left top image shows the correlation spectrum of BATSE data for $t < 2$ sec and CMB without consideration for the mask. The right top image contains the correlation spectrum of the BATSE data with $t > 2$ sec and CMB without consideration for the mask. The bottom left image demonstrates the correlation spectrum of the BATSE data for $t < 2$ sec and CMB with consideration for the mask. The right bottom image shows the correlation spectrum of the BATSE data with $t > 2$ sec and CMB with consideration for the mask. The images show the 1σ -dispersion obtained from results of analysis of 200 Gaussian random realizations of CMB.

examples of such harmonics. The fourth multipole of mosaic correlation map with the window $500' \times 500'$ calculated for the BATSE data ($t < 2$ sec) contains a feature — the coldest central spot in the galactic plane (Fig. 17, left top). Quadrupole of the correlation map for the BATSE data ($t > 2$ sec) with the window $900' \times 900'$ (Fig. 17, left bottom) is sensitive to the equatorial coordinate system. Note that the change of correlation scale (namely, the size of area in which the correlation factor is calculated and attributed to a pixel of mosaic

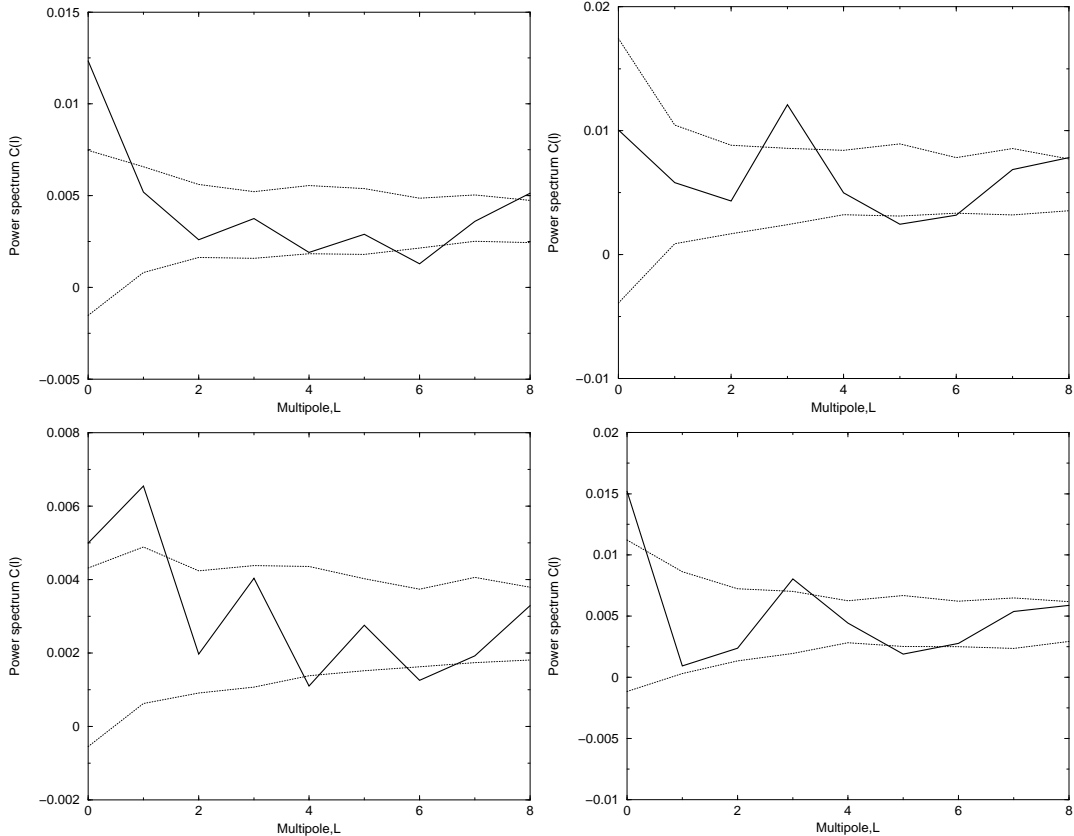


Figure 15. Power spectra of correlation maps (with the resolution of $\ell_{\max} = 8$) calculated for the maps of BATSE GRBs locations and CMB distribution (the solid line). The correlation pixel size is $600' \times 600'$. The left top image shows the spectrum of correlation map for the BATSE data (GRBs with $t < 2$ sec) and CMB without masking. The right top image contains the correlation spectrum of the BATSE data for $t > 2$ sec and CMB without masking. The bottom left image demonstrates the correlation spectrum of the BATSE data for $t < 2$ sec and CMB with masking. The right bottom image shows the correlation spectrum of BATSE data for $t > 2$ sec and CMB with masking. The images show the 1σ dispersion obtained from results of analysis of 200 Gaussian random realizations of CMB.

map) changes the power spectrum. Thus, e.g., at transition from the pixel side of size $500'$ to that of $600'$ the harmonic $\ell = 4$ amplitude in the power spectrum passes from position of a local maximum to a local minimum. This can be caused by the increase of amount of GRB events in the area of corresponding size.

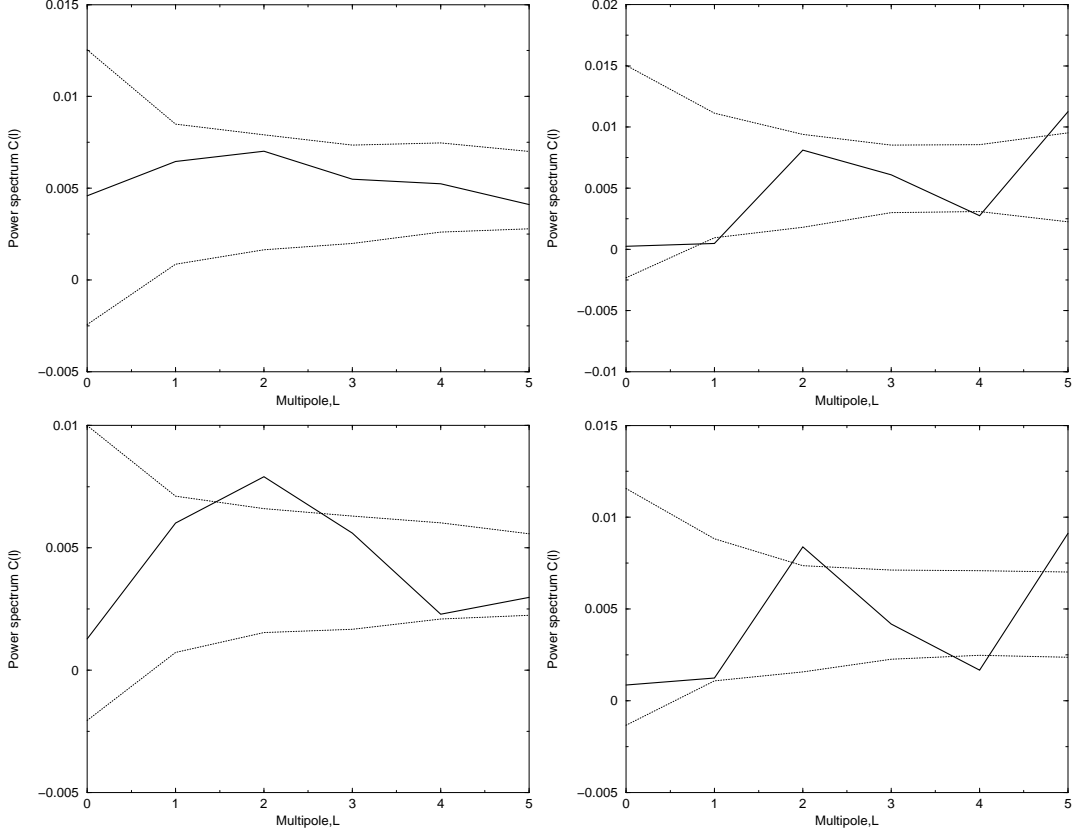


Figure 16. Power spectra of mosaic correlation maps with the resolution of $\ell_{\max} = 5$ for the maps of BATSE GRB locations and CMB distribution (the solid line). The correlation pixel size is $900' \times 900'$. The left top image shows the correlation spectrum of the BATSE data ($t < 2$ sec) and CMB without masking. The right top image contains the correlation spectrum of the BATSE data with $t > 2$ sec and CMB without masking. The bottom left image demonstrates the correlation spectrum of the BATSE data with $t < 2$ sec and CMB with masking. The right bottom image shows the correlation spectrum of the BATSE data for and CMB with masking. The images show the 1σ dispersion obtained from results of analysis of 200 Gaussian random realizations of CMB.

4. THE AVERAGING OF FIELDS

The Planck data allow us using the maps of higher resolution than the WMAP archives. They can be applied to estimate a potential signal from “an average population GRB”.

To do that, areas of an identical linear or angular size around objects under investigation are selected in different directions on the celestial sphere. Then they are summed up to reveal an average signal. Because data on red shifts are not available, we used areas with identical angular sizes. To avoid influence of a possible hard-to-consider signal of the Galaxy

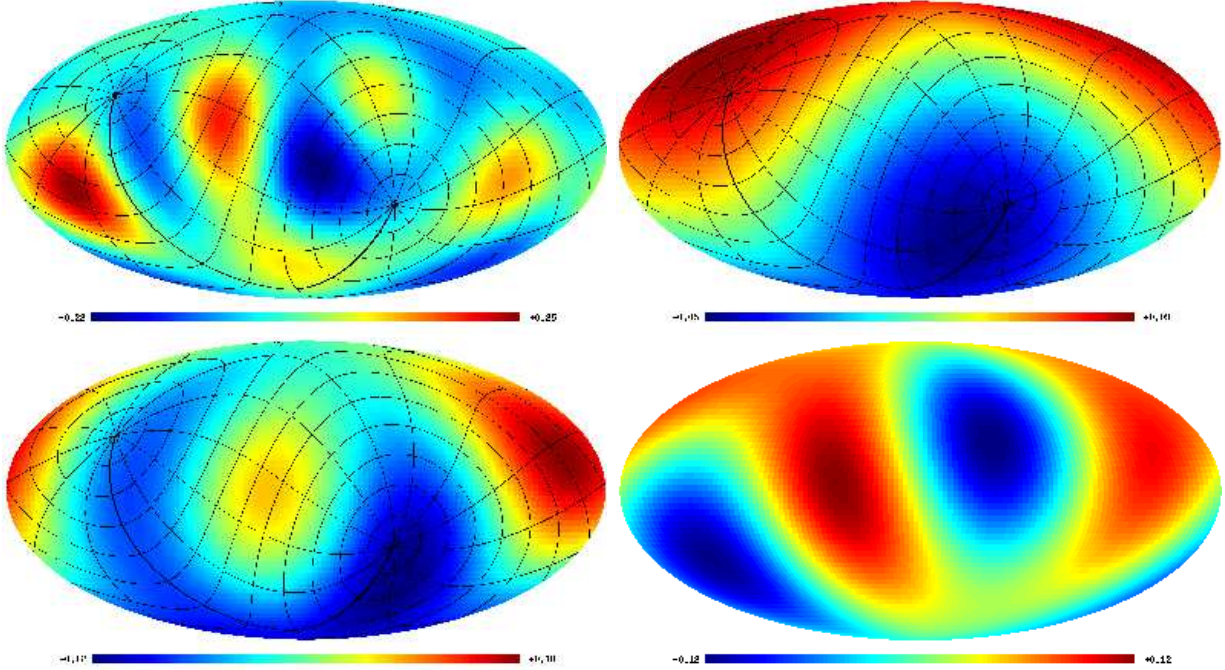


Figure 17. Maps of distinguished harmonics in power spectra (Fig. 14,15,16). The images show multipoles of mosaic correlations of CMB and GRB locations. Top left: the distinguished harmonics $\ell = 4$ for the correlation window $500' \times 500'$ for BATSE data ($t < 2$ sec); top right: the distinguished harmonic $\ell = 1$ for the correlation window $600' \times 600'$. Bottom left: the correlation map for BATSE GRBs ($t < 2$ sec) and CMB with the correlation window $900' \times 900'$ ($\ell = 2$). Bottom right: the correlation map for BATSE GRBs ($t > 2$ sec) and CMB with the correlation window $900' \times 900'$ ($\ell = 2$). The third map contains the overlaid equatorial coordinate grid.

we limited ourselves only to regions around GRBs with galactic latitudes $|b| > 20^\circ$. Among BATSE and BeppoSAX samples, this range includes 338 short (68% of the initial short BATSE GRBs) and 990 (64%) long events of the BATSE catalog, and 51 short (59% of the BeppoSAX list) and 454 (65%) long sources of the BeppoSAX catalog. For every GRB from our subsample we have chosen a field in the Planck SMICA map of size $2^\circ \times 2^\circ$ in the tangential projection (the pixel size in the area is $\sim 80'' \times 80''$). The selected areas were averaged. Results are shown in Fig. 18. Note that the addition of data from the region $|b| < 20^\circ$ leads to degradation (blurring) of images.

The center of each averaged field in Fig. 18 gets to a region of a local extremum. Short BATSE and BeppoSAX GRBs are in regions of a background minimum, and the long ones – in regions of a maximum. Ratios of a level of averaged fluctuation of an extremum to which

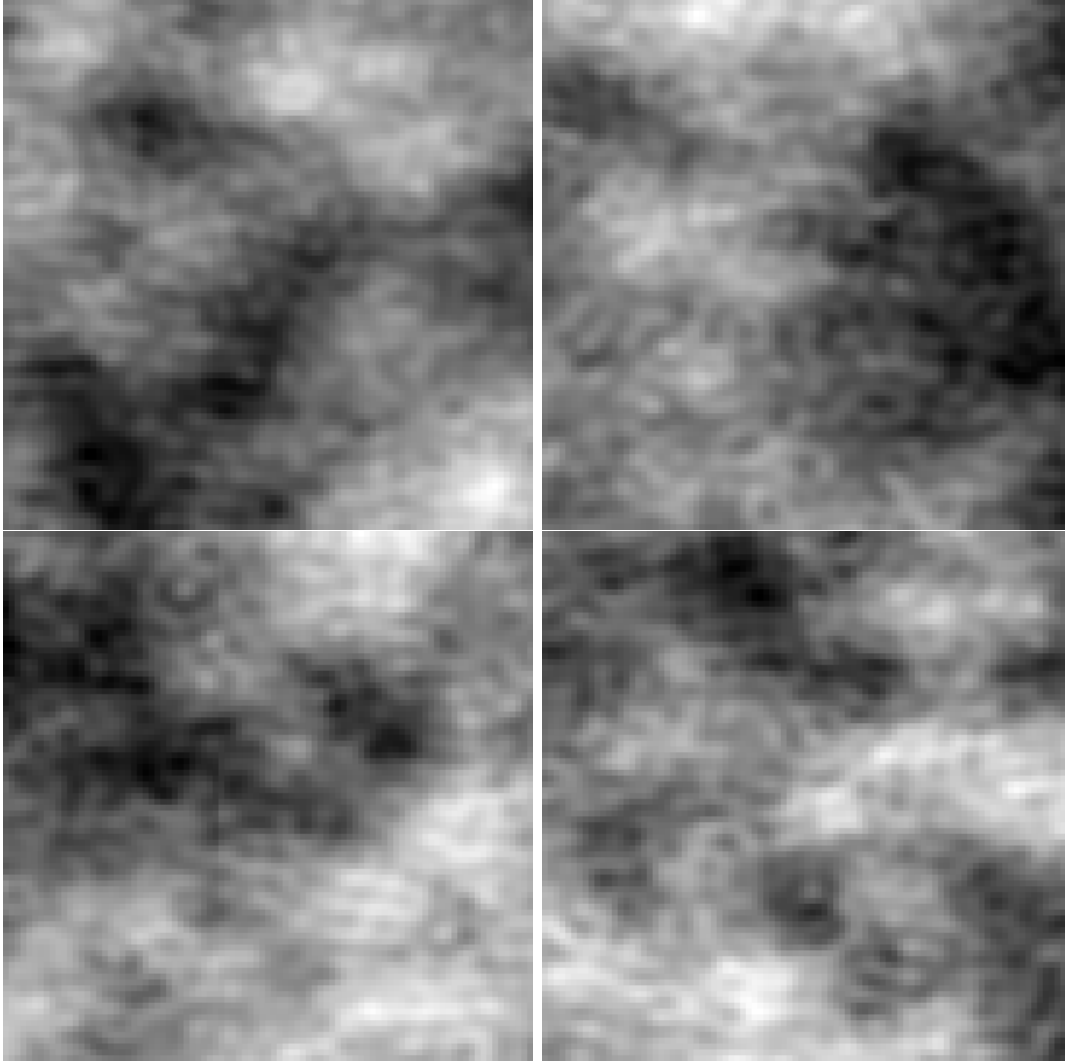


Figure 18. Results of the averaging of CMB fields of size $2^\circ \times 2^\circ$ in GRB directions. From left to right downward: fields of short BATSE GRBs; long BATSE GRBs; short and long BeppoSAX GRBs.

a generalized GRB gets to a level of noise on averaged maps are $dS/N = -1.65, 1.40, -1.43, 2.01$ $1.40, -1.43, 2.01$ for short and long BATSE GRBs and short and long BeppoSAX GRBs respectively.

5. DISCUSSION

In this paper we investigated the CMB signal statistics in direction of GRBs from the BATSE and BeppoSAX cataloges. The Planck SMICA map was used as the CMB map. We applied three approaches to the study of properties of the sphere distribution of GRBs. They includes: 1) analysis of the histogram of Planck CMB signal values in direction to GRBs, 2)

the study of mosaic maps built for GRB locations and CMB distribution, 3) the study of an average response on the CMB map in the region of an “average population GRB”.

Application of the first two methods demonstrates that the correlation between GRB and CMB is caused, at least partially, by a signal in the equatorial coordinate system. This agrees with results of our previous work [24]. This relation can be caused by modulation of the CMB signal observed in the point L2 by microwave radiation of the Earth through the far antenna beam lobes. Deviations in distribution of GRBs towards the equatorial system are caused by non-uniform sky sensitivity (the time of signal accumulation) of the receiving equipment of gamma-ray satellite observatories rotating around the Earth and always directed at the opposite side from it. Then a distinguished character of the equatorial coordinate system appears naturally. Note that indication to the presence of signs of the equatorial coordinate system (e.g., location of equatorial spots) in CMB data both for WMAP and Planck maps was already discussed in a number of papers [24, 32, 33]. Besides, radiation of the Earth can be not a single factor. Another discussed reason can be the modulation of the solar wind by the Earth magnetic field passing through the point L2. It should be added that such effects which are not detectable by the standard analysis could be a source of the secondary gaussianity observed at low harmonics [34–38].

The third method applied by us has shown that there is an insignificant difference at the level $|S/N| > 1.4$ which can randomly occur in $\lesssim 20\%$ cases for the Gaussian noises in distribution of average CMB signal in GRB directions. As this takes place, short ($t < 2$ sec) GRBs in an averaged field gets to a local background minimum, and long ($t > 2$ sec) GRBs – to a local maximum. If we assume that short GRBs arise in old elliptic galaxies formed from merging less massive galaxies and located in galaxy clusters, then a local minimum can be due to the Zeldovich–Syunyaev effect [3]. The getting of long GRBs to a local maximum of CMB distribution could be caused by another effect. If long GRBs are related to supernovae explosions, i.e. with starforming galaxies, then even in spite of location in a galaxy cluster the proper microwave emission of a galaxy containing dust and gas would prevail over effects of surrounding and lead to appearance of a local maximum in CMB maps. This effect could be tested by means of more sensitive data of the Planck experiment in the next publication release which is expected in the second half of 2014.

Acknowledgments. The authors are grateful to EAS for the open access to results of obser-

vations and processing of data in Planck Legacy Archive. The authors thank T.N.Sokolova for reading, correcting and translating this text. For analysis of extended emission on sphere we used the package GLESP [31, 39, 40]. M.L.Kh. and O.V.V. thank RFBR for a partial support of the project study by the RFBR grant 13-02-00027.

-
1. D. J. Eisenstein, D. H. Weinberg, E. Agol, et al., *AJ* **142**, 72 (2011), arXiv:1101.1529.
 2. R. K. Sachs and A. M. Wolfe, *ApJ* **147**, 73 (1967).
 3. R. A. Sunyaev and Ya. B. Zeldovich, *Astrophys. Sp. Sci.* **7**, 3 (1970).
 4. P. J. E. Peebles, *Principles of Physical Cosmology* (Princeton Univ. Press, 1993).
 5. J. A. Peacock, *Cosmological Physics* (Cambridge Univ. Press, 2000).
 6. L. Rudnick, S. Brown, and L. R. Williams, *Astrophys. J* **671**, 40 (2007).
 7. V. Springel, C. S. Frenk, and S. D. M. White, *Nature* **440**, 1137 (2006).
 8. J. Yadav, S. Bharadwaj, B. Pandey, and T. R. Seshadri, *MNRAS* **364**, 601 (2005), astro-ph/0504315
 9. P. Sarkar, J. Yadav, B. Pandey, and S. Bharadwaj, *MNRAS* **399**, L128 (2009).
 10. F. Sylos Labini and Y. V. Baryshev, *JCAP* **6**, 021 (2010).
 11. W. A. Watson, I. T. Iliev, J. M. Diego, et al., *MNRAS* **437**, 3776 (2014), arXiv:1305.1976.
 12. Ya. V. Naiden and O. V. Verkhodanov, *Astrophys. Bull.* **68**, 471 (2013).
 13. J. F. Navarro, C. S. Frenk, and S. D. M. White, *ApJ* **490**, 493 (1997), astro-ph/9611107.
 14. M. L. Khabibullina and O. V. Verkhodanov, *Astronomy Reports* **55**, 302 (2011), arXiv:1108.4506.
 15. L. Amati, et al., *Astronom. and Astrophys.* **390**, 81 (2002).
 16. L. Amati, et al., *Monthly Notices Roy. Astronom. Soc.* **391**, 557 (2008).
 17. D. Riccia, F. Fioreb, and P. Giommia, *Nuclear Physics B - Proc. Suppl.* **69**, 618 (1999).
 18. W. S. Paciesas, C. A. Meegan, G. N. Pendleton, et al. McCollough, *Astrophys. J. Suppl.* **122**, 465 (1999), astro-ph/9903205.
 19. R. Vavrek, et al., in “A Workshop Celebrating the First Year of the HETE Mission”, *AIP Conf. Proc.* **662**, 163 (2003).
 20. L. L. R. Williams and N. Frey, *Astrophys. J* **583**, 594 (2003).
 21. A. Mészáros and J. Stoeck, *Astro. & Astrophys.* **403**, 443 (2003), astro-ph/0303207.

22. A. Bernui, I. S. Ferreira, and C. A. Wuensche, *Astrophys. J* **673**, 968 (2008), arXiv:0710.1695.
23. A. Mészáros, L. G. Balázs, Z. Bagoly and P. Veres, *GAMMA-RAY BURST: Sixth Huntsville Symposium*, AIP Conf. Proc. **1133**, 483 (2009), arXiv:0906.4034.
24. O. V. Verkhodanov, V. V. Sokolov, M. L. Khabibullina and S. V. Karpov, *Astrophys. Bull.* **65**, 238 (2010), arXiv:1009.3720.
25. V. N. Yershov, V. V. Orlov, and A. A. Raikov, *MNRAS* **423**, 2147 (2012).
26. O. V. Verkhodanov, M. L. Khabibullina and E. K. Majorova, *Astrophys. Bull.* **64**, 263 (2009).
27. O. V. Verkhodanov and M. L. Khabibullina, *Astrophys. Bull.* **65**, 390 (2010).
28. N. Jarosik, C. L. Bennett, J. Dunkley, et al., *Astrophys. J. Supp.*, submitted (2010), arXiv:1001.4744.
29. Planck Collaboration: P. A. R. Ade, et al., *Astronom. and Astrophys.*, submitted (2013), arXiv:1303.5062.
30. Planck Collaboration: P. A. R. Ade, et al., *Astronom. and Astrophys.*, submitted (2013), arXiv:1303.5072.
31. A. G. Doroshkevich, O. B. Verkhodanov, P. D. Naselsky, et al., *Intern. J. Mod. Phys.* **20**, 1053 (2011), arXiv:0904.2517.
32. O. V. Verkhodanov, *Astrophys. Bull.* **69**, accepted (2014).
33. Ya. V. Naiden, O. V. Verkhodanov, *Astrophys. Bull.* **69**, accepted (2014).
34. A. Rakic and D. J. Schwarz, *Phys. Rev. D* **75**, 103002 (2007).
35. Ja. Kim and P. Naselsky, *Phys. Rev D* **82**, 063002 (2010).
36. O.V. Verkhodanov, *Phys. Usp.* **55**, (2012).
37. M. Hansen, J. Kim, A. M. Frejsel, et al., *JCAP* **10**, 059 (2012).
38. C. J. Copi, D. Huterer, D. J. Schwarz, and G. D. Starkman, arXiv:1311.4562 (2013).
39. A. G. Doroshkevich, P. D. Naselsky, O. V. Verkhodanov et al., *Int. J. Mod. Phys.* **14**, 275 (2003), astro-ph/0305537.
40. O. V. Verkhodanov , A. G. Doroshkevich, P. D. Naselsky, et al., *Bull. SAO* **58**, 40 (2005).